

Multiplierless Filtered-OFDM Transmitter for Narrowband IoT Devices

AlaaEddin Loulou, Juha Yli-Kaakinen, Toni Levanen, Vesa Lehtinen, Frank Schaich, Thorsten Wild, Markku Renfors, and Mikko Valkama

Abstract—In cyclic-prefix orthogonal frequency-division multiplexing (CP-OFDM) based radio access, the coexistence of different technologies without precise time-frequency synchronization is limited due to high out-of-band emissions. Therefore, spectrum enhancement techniques play a key role to relax the synchronization and power control requirements. This allows higher degree of opportunistic spectrum use with minimized interference. In addition, all transmitting devices have to fulfill specific transmitted signal quality requirements, including the maximum out-of-band radiated signal power. With OFDM based radio access, some additional signal processing for improved spectrum containment is commonly needed to achieve these requirements. Filtering and time-domain windowing are two fundamentally different approaches for spectrum enhancement. Filtered OFDM (F-OFDM) provides better spectrum localization than the time-windowing schemes (such as windowed overlap-add, WOLA), with the cost of higher complexity. This paper introduces low-complexity solutions for spectrally enhanced narrowband OFDM transmitters based on the use of a look-up tables (LUTs). The proposed LUT approach, requiring only memory units and a low number of additions, allows to avoid all computationally expensive operations in on-line transmitter processing, as it builds the transmitted signal by summing the stored partial waveforms optimized off-line. In certain cases, completely multiplication and summation free designs are possible. The transmitters of narrowband Internet of things (NB-IoT) devices are natural applications for the proposed LUT approach, as they require additional digital baseband signal processing to reach the emission requirements. It is shown that the proposed LUT schemes can provide significant savings in real-time computations of NB-IoT devices, while fulfilling the 3GPP requirements.

Index Terms—IoT, NB-IoT, multicarrier waveforms, OFDM, DFT-s-OFDM, fast Fourier transforms, filtered OFDM, WOLA, 5G New Radio, look-up-table, LUT

I. INTRODUCTION

The continuous development in the communication systems foresees the connection of all devices, such as home and industrial appliances, as an essential part of the future generation networks. This idea is widely known as Internet-of-things (IoT) [2], [3]. IoT aims at connecting large number of devices over wireless or wired networks. This paper considers wide-area low-power narrowband scenarios for wireless IoT. Here,

a massive amount of devices is to be connected to the wireless network, transmitting/receiving sporadically messages with small payloads. This is called massive machine-type communication (mMTC). Accordingly, the 3rd generation partnership project (3GPP) has introduced a new radio interface called narrowband IoT (NB-IoT) mainly for long term evolution (LTE) networks, but also applicable in the global system for mobile communications (GSM) frequency bands. NB-IoT is based on the existing LTE functionalities targeting at ultra-low complexity devices with wide coverage, supporting massive number of MTC devices and improved power efficiency [4]–[7]. The NB-IoT channel can be deployed outside the LTE spectrum in the stand-alone option. Alternatively, NB-IoT can be deployed either within the active resource blocks of the LTE system or within the guard-bands between active LTE resource blocks and channel edge; these are called in-band and guard-band deployment options, respectively. In all these options, the interference with coexisting technologies, such as GSM and LTE, should be minimized.

LTE adopts cyclic-prefix orthogonal frequency-division multiplexing (CP-OFDM) for downlink. On the other hand, the uplink uses discrete Fourier transform-spread-OFDM (DFT-s-OFDM), also known as single-carrier frequency-division-multiple-access (SC-FDMA), to mitigate the peak-to-average power ratio (PAPR). Generally, CP-OFDM and DFT-s-OFDM exhibit high-power spectral sidelobes potentially leaking to the neighboring parts of the spectrum. This is critical especially in the 5G New Radio (5G-NR), which extends the LTE numerology by allowing different subcarrier spacings (SCSs) in adjacent subbands [8]. This is referred to as mixed numerology and it causes inter-numerology interference since the OFDM subcarriers with different SCSs are not orthogonal in general. In order to reduce the interference leakage between subbands with different numerologies, 3GPP has allowed subband-based spectral enhancement techniques to be used, but these should be transparent to the receiver [9].

In general, spectrum enhancement methods to suppress the spectral sidelobes are required in OFDM-based radio communication systems in order to satisfy their specific out-of-band emission requirements. Concerning NB-IoT, these requirements are defined in the 3GPP specification [10]. The related difficulties in guard-band and in-band deployments are discussed in [6], [11] and according to [11], the channel filtering challenges limit the deployment of NB-IoT with LTE carrier bandwidths smaller than 5 MHz. It is also indicated in [11] that with a standard-complying interference leakage model, up to 4.7 % throughput loss may be observed in the

A. Loulou, J. Yli-Kaakinen, T. Levanen, V. Lehtinen, M. Renfors, and M. Valkama are with the Faculty of Information Technology and Communication Sciences, Tampere University, P.O. Box 692, FI-33101 Tampere, Finland (e-mail: alaa.loulou@tuni.fi; juha.yli-kaakinen@tuni.fi; toni.levanen@tuni.fi; vesa.lehtinen@tuni.fi; markku.renfors@tuni.fi; mikko.valkama@tuni.fi)

F. Schaich, T. Wild are with Nokia Bell Labs, Germany (e-mail: frank.schaich@nokia-bell-labs.com; thorsten.wild@nokia-bell-labs.com)

This work was supported by Business Finland and Nokia Bell Labs under the Wireless for Verticals (WiVe) project. Early stage results of this study have been published in Proceedings of ISWCS 2019 [1].

host LTE uplink. Effective NB-IoT filtering techniques can be expected to relax these issues. NB-IoT with some enhancements is also considered as one of the mMTC solutions for 5G-NR [12]. In this context, the demand for NB-IoT sidelobe suppression becomes particularly important. Regarding uplink transmission, generally, improved spectrum localization makes the system more tolerant to synchronization errors and imperfect power control. Asynchronous (grant-free) uplink operation makes sporadic short packet transmission effective in terms of synchronization overhead, and is considered as an important element in the further development of 5G-NR. In summary, effective techniques for enhancing the NB-IoT spectrum localization are needed both for satisfying the current specifications, and for enhanced performance and coexistence in NB-IoT evolution in the 5G-NR and beyond.

Numerous different schemes have been proposed for OFDM spectrum enhancement, i.e., for suppressing the sidelobes. In 5G-NR developments, a time-domain windowing approach, referred to as windowed overlap and add (WOLA) [13], and subband-wise filtered OFDM (F-OFDM) [14]–[17] have been mainly considered. Generally, F-OFDM has better performance although higher complexity. F-OFDM is able to provide good spectrum localization for CP-OFDM physical resource blocks (PRBs) or groups of PRBs. Recently, the high flexibility and low complexity of fast-convolution (FC) based F-OFDM has been demonstrated in 5G-NR scenarios in [18] and it has been considered for IoT applications in [17]. Also simplified FC processing structure for narrowband user equipments (UEs) has been reported [19]. The combination of FC and WOLA processing has been considered for 5G uplink in [20].

NB-IoT devices target at extremely low implementation and on-line computation complexity, and both time- and frequency-domain digital filters may be considered too complex, as indicated also by the numerical results of Section V-B below. It will be seen that the WOLA technique is not able to satisfy 3GPP emission requirements in all NB-IoT uplink configurations. In addition, it may compromise the link performance in highly dispersive channels since time domain windowing reduces the effective CP length.

In this paper, we propose an advanced implementation variant for F-OFDM and filtered DFT-s-OFDM (DFT-s-OFDM-F) with extremely low on-line computational complexity. It is suitable for narrowband uplink transmission, i.e., for the transmitter of an ultra-low cost mMTC device, *requiring no multiplications in scenarios like the NB-IoT uplink*. This new scheme stores the complex time-domain samples of the filtered modulated symbols for each transmitted input symbol or group of input symbols in a look-up table (LUT) [21], [22]. Then the transmitted sample vector is selected from the LUT based on the input data symbols. This scheme avoids also the computationally intensive DFT and IFFT processing, making it possible to do the digital waveform generation without any multiplications. The waveform can be pre-optimized for each use case or scenario separately, depending, e.g., on the spectral containment requirement or synchronization accuracy. LUT-based processing can be applied also for the WOLA scheme, but its complexity benefit over LUT-based F-OFDM is relatively small, as will be shown in Section V.

The main contributions of this paper can be listed as follows:

- The LUT approach is defined for multiplication-free NB-IoT signal generation. The LUT sizes and addition rates of different variants of the LUT scheme are compared and realistic configurations are identified. The computational complexity of LUT-based scheme is also compared with time- and frequency-domain F-OFDM approaches.
- Analytical expressions are developed for LUT contents, signal modeling, and computational complexity. While the case studies focus on NB-IoT, the developed schemes and models are generally applicable to narrowband filtered OFDM and DFT-s-OFDM transmitters.
- We develop a technique to deal with the CP length variations without increasing the computational complexity or memory requirements.
- A simplified technique to address the stored waveforms for groups of input symbols in the LUT is presented.
- A completely multiplication and addition free scheme is proposed for narrow (1 or 3 subcarrier) allocations.
- LUT wordlengths required to meet the 3GPP specifications are evaluated for different LUT variants, considering also the effects of a practical power amplifier model.
- LUT approach for multiplication free WOLA-based OFDM and DFT-s-OFDM signal generation is proposed and compared with the LUT-based F-OFDM scheme.
- It is demonstrated through link-level evaluations of a LTE guard-band deployment case that the LUT-OFDM approach is able to significantly reduce the interference leakage between NB-IoT and the host LTE system. It is shown that applying filtering in both LTE and NB-IoT systems allows to achieve the link error-rate performance of the corresponding radio links without interference.

This paper is arranged as follows. Section II gives a short overview of NB-IoT. Section III presents the filtered or windowed DFT-s-OFDM transmitter model as a basis for the LUT scheme developments. Section IV develops new implementation variants based on LUT. This scheme is applicable to both filtering and windowing based OFDM and DFT-s-OFDM, and the scheme is referred to as LUT-OFDM. Our focus in the developments is on filtered DFT-s-OFDM, but the extensions are straightforward. After explaining the basic form of LUT-OFDM, three enhanced variants (input symbol grouping, CP extrapolation, and stored symbol transitions) are presented. Section V begins with an example demonstrating the benefits of filtering for both LTE and NB-IoT link performance in asynchronous NB-IoT guard-band deployment. Then we compare the memory requirements and computational complexity of the LUT-OFDM variants and the basic filtering and windowing schemes, first in generic terms. Then the specific aspects related to the NB-IoT uplink are addressed. The memory wordlengths required to reach the 3GPP specifications for in-band distortion and out-of-band emissions [10] are evaluated by simulations, considering also the effects of a practical nonlinear power amplifier model. Finally, concluding remarks are presented in Section VI. Some essential notations and parameters are listed in Table I.

II. NB-IoT OVERVIEW

The LTE standard uses CP-OFDM and DFT-s-OFDM schemes for downlink and uplink, respectively [23]. The standard offers a variety of bandwidth configurations from 1.4 MHz up to 20 MHz. Accordingly, with 15 kHz SCS and 12 subcarrier PRB size, the use of 6, 15, 25, 50, 75, and 100 PRBs per channel requires FFT sizes of 128, 256, 512, 1024, 1536, and 2048, respectively. Considering LTE with frequency-division duplexing (FDD), time resources are divided into radio frames of 10 ms. Each frame is divided into 10 subframes, each of which is further divided into two slots. The slot contains 6 OFDM symbols for extended CP configuration and 7 OFDM symbols for normal CP configuration. In the normal CP configuration, the first CP is slightly longer to maintain exactly 0.5 ms duration per slot.

NB-IoT is implemented using the LTE parameters with normal CP [6]. Basically, an NB-IoT channel uses up to 180 kHz of the spectrum. This is equivalent to one LTE PRB of 12 subcarriers. For uplink, 1, 3, 6 or 12 subcarriers can be assigned to a UE with 15 kHz SCS and 3.75 kHz SCS is also supported in single-tone transmission. Each transmission event uses at least one subframe with varying number of slots depending on the number of assigned subcarriers for the UE uplink. In the case of single subcarrier allocation (single-tone uplink), phase-rotated constellations $\pi/2$ -BPSK and $\pi/4$ -QPSK are used instead of basic BPSK and QPSK. In multi-tone transmission, only QPSK modulation is supported by the NB-IoT specifications. However, to extend the parameter set beyond the current specifications, BPSK modulation for multi-tone case is also considered in this document. Moreover, the choice of normal vs. extended CP is included in the discussions, even though only normal CP configuration is supported in the specifications [24]. The focus in this document is on the uplink side with 15 kHz SCS.

The NB-IoT baseband system model assumes that the 12 subcarriers of the PRB are located symmetrically around the zero-frequency (DC), i.e., the carrier frequencies are $(k+0.5)\Delta f$, where the subcarrier indices are $k = -6, -5, \dots, 5$ and $\Delta f = 15$ kHz is the subcarrier spacing.

III. FILTERED DFT-S-OFDM TRANSMITTER MODEL

DFT-s-OFDM is an OFDM-based single-carrier transmission scheme, where each data symbol block of length B is first frequency-spread by a DFT of length B . Then the spread data is allocated to B subcarriers of an OFDM modulator that is implemented by inverse fast Fourier transform (IFFT). A CP of length N_{cp} is prepended to the IFFT output in the usual way. This is followed by the subband filtering process used suppressing the out-of-band sidelobes. Here we follow the uplink orthogonal frequency-division multiple access (OFDMA) baseband model in which the users are allocated to alternative sets of contiguous subcarriers. A fixed lowpass filter, independent of used allocation, is assumed. The output signal is generated with significant oversampling, and the filter bandwidth corresponds to the channel bandwidth (180 kHz in the NB-IoT case).

TABLE I
IMPORTANT SYMBOLS AND NOTATIONS

Notation	Meaning
$W_k = \exp(-2\pi j/k)$	DFT twiddle factor, k th complex root of unity
\mathbf{I}_k	$k \times k$ identity matrix
$\mathbf{0}_{k \times p}$	$k \times p$ zero matrix
$\lfloor x \rfloor$	Floor operation: greatest integer $\leq x$
$\langle n \rangle_k$	Modulo operation: $\langle n \rangle_k = n - k \lfloor n/k \rfloor$
$(c^{(A)})_{p,q}$	Element-wise matrix power of \mathbf{A}
B -DFT	DFT of length B
B	Input symbol block length
N	OFDM transform size
$a_{b,n}$	b th input symbol for n th OFDM symbol
$\mathbf{w}_{B \times 1}^{(b)}$	DFT vector for b th input symbol
$\mathbf{W}_{N \times B}^{(k_0)}$	Odd IDFT matrix for B subcarriers centered at k_0
$\mathbf{C}_{N_s(n) \times N}^{(n)}$	CP insertion matrix for n th OFDM symbol
$\mathbf{H}_{N_c(n) \times N_s(n)}^{(n)}$	Filtering matrix for n th OFDM symbol
$\mathbf{q}_{N_s(n) \times 1}^{(b,n)}$	Time-domain DFT-s-OFDM response
$\mathbf{f}_{N_c(n) \times 1}^{(b,n)}$	Time-domain DFT-s-OFDM-F response

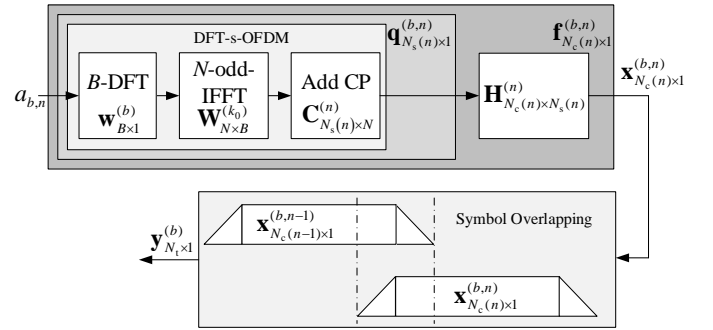


Fig. 1. The DFT-s-OFDM-F transmitter model for a single input symbol, used as a basis for developing the LUT scheme. The actual output is the sum of waveforms produced by the B input symbols.

Considering the varying CP length, the values of the CP length and other related parameters are defined in the following generic analyses as a function of the DFT-s-OFDM-F symbol index n , i.e., $N_{cp}(n)$, $N_s(n)$, etc. Here $n = [0, 1, \dots, N_f - 1]$, where N_f is the total number of DFT-s-OFDM-F symbols within a subframe, and $N_s(n)$ is the length of the DFT-s-OFDM-F symbol that includes the length of the IFFT output samples N and CP samples $N_{cp}(n)$. The CP length variation in the normal CP configuration of LTE occurs only in the first CP in the slot whilst the remaining 6 symbols in the slot have equal lengths. In this context we use a simplified notation for the lengths, i.e., \hat{N}_{cp} , \hat{N}_s , etc. for the first symbols and N_{cp} , N_s for the other symbols.

The time-domain filtering based structure of DFT-s-OFDM-F transmitter for a single input symbol is shown in Fig. 1. The single input symbol model of the DFT-s-OFDM-F is adopted in here because it is useful for the following discussions of LUT-OFDM. Nevertheless, the actual implementation of the DFT-s-OFDM-F performs the sum of the waveforms produced

for each of the B subsymbols of the input data block. The output of the block-wise filtering stage due to a single input symbol (without considering the overlapping between the consecutive DFT-s-OFDM-F symbols due to filtering) is

$$\mathbf{x}_{N_c(n) \times 1}^{(b,n)} = \mathbf{f}_{N_c(n) \times 1}^{(b,n)} a_{b,n}, \quad (1)$$

where $b = [0, 1, \dots, B-1]$ is the index of the input data symbol to the spreading B -DFT, and $a_{b,n}$ is the b th input data symbol of n th DFT-s-OFDM-F symbol block. The length of the acyclic convolution (also known as linear convolution) of the DFT-s-OFDM-F symbol with the N_h -point impulse response is $N_c(n) = N_s(n) + N_h - 1$. In (1), $\mathbf{f}_{N_c(n) \times 1}^{(b,n)}$ is the DFT-s-OFDM-F processing vector expressed as

$$\mathbf{f}_{N_c(n) \times 1}^{(b,n)} = \mathbf{H}_{N_c(n) \times N_s(n)}^{(n)} \mathbf{q}_{N_s(n) \times 1}^{(b,n)}. \quad (2)$$

Here, $\mathbf{H}_{N_c(n) \times N_s(n)}^{(n)}$ is the acyclic convolution matrix for low-pass filtering and $\mathbf{q}_{N_s(n) \times 1}^{(b,n)}$ is defined as

$$\mathbf{q}_{N_s(n) \times 1}^{(b,n)} = \mathbf{C}_{N_s(n) \times N}^{(n)} \mathbf{W}_{N \times B}^{(k_0)} \mathbf{w}_{B \times 1}^{(b)}, \quad (3)$$

where $\mathbf{w}_{B \times 1}^{(b)}$ is the spreading DFT vector of length B for the b th input that expressed as follows:

$$\mathbf{w}_{B \times 1}^{(b)} = \left[1 \ W_B^b \ \dots \ W_B^{b(B-1)} \right]^T. \quad (4)$$

In (3), $\mathbf{W}_{N \times B}^{(k_0)}$ is a modified IDFT matrix with inputs of length B and k_0 is the first (lowest) subcarrier of the allocation. It is convenient to assume the subcarrier index range of $[-N/2, N/2-1]$ while the IDFT length N takes an even value in practice. The matrix $\mathbf{W}_{N \times B}^{(k_0)}$ consists of the columns of the odd IDFT matrix corresponding to the used allocation and it can be expressed as

$$\left(\mathbf{W}_{N \times B}^{(k_0)} \right)_{(l+1)(b+1)} = W_N^{-l(k_0+b)} W_N^{-0.5l}, \quad (5)$$

where $l+1$ and $b+1$ are the matrix row and column indices, respectively, and $l = 0, 1, \dots, N-1$ is the output index of the N -odd-IDFT. Here the first term is the IDFT for the specific user allocation and the second term shifts the signal spectrum by half of the subcarrier spacing. Depending on the system specifications, the latter term may be absent, in which case (5) consists of selected rows of the basic IDFT matrix.

In (3), $\mathbf{C}_{N_s(n) \times N}^{(n)}$ is the CP insertion matrix for the DFT-s-OFDM-F symbol that can be expressed as follows:

$$\mathbf{C}_{N_s(n) \times N}^{(n)} = \begin{bmatrix} \mathbf{0}_{N_{cp}(n) \times (N-N_{cp}(n))} & \mathbf{I}_{N_{cp}(n)} \\ & \mathbf{I}_N \end{bmatrix}. \quad (6)$$

The baseband signal for the whole subframe is created by adding up the waveforms generated for each input symbol of each DFT-s-OFDM-F block and by using overlap-and-add for consecutive filtered DFT-s-OFDM-F symbols as follows:

$$\mathbf{y}_{N_t \times 1} = \sum_{b=0}^{B-1} \mathbf{y}_{N_t \times 1}^{(b)} = \sum_{b=0}^{B-1} \sum_{n=0}^{N_t-1} \mathbf{S}_{N_t \times N_c(n)}^{(n)} \mathbf{x}_{N_c(n) \times 1}^{(b,n)}. \quad (7)$$

Here $\mathbf{S}_{N_t \times N_c(n)}^{(n)}$ is a shift matrix that rearranges the DFT-s-OFDM-F symbols for overlap-and-add and it is expressed as

$$\mathbf{S}_{N_t \times N_c(n)}^{(n)} = [\mathbf{0}_{N_c(n) \times N_v(n)} \ \mathbf{I}_{N_c(n)} \ \mathbf{0}_{N_c(n) \times N_c(n)}]^T, \quad (8)$$

where $N_v(n)$ is the shift of the n th DFT-s-OFDM-F symbol in the subframe and it is expressed as

$$N_v(n) = \sum_{r=0}^n N_s(r-1), \quad (9)$$

with $N_s(-1) = 0$ and $N_c(n)$ is the length of the remaining unused parts of the subframe that is defined as

$$N_c(n) = N_t - N_v(n) - N_c(n), \quad (10)$$

and N_t is the total number of the modulated samples in the subframe that is defined as follows:

$$N_t = \left(\sum_{n=0}^{N_t-1} N_s(n) \right) + N_h - 1. \quad (11)$$

In this section, a generic model for DFT-s-OFDM-F signal generation was formulated. For the NB-IoT case, we assume that the transmission channel of 12 subcarriers is symmetric around DC and, therefore, the half-subcarrier-shift was introduced in (5), following the 3GPP specifications [24]. This allows to use a conventional lowpass filter with real-valued impulse-response coefficient values, with a bandwidth corresponding to the channel width, for all user allocations.

The general model of this section applies also for a single subcarrier of filtered CP-OFDM, with or without half-subcarrier frequency shift, just the spreading transform (B -DFT) is absent, and Eq. (3) is replaced by

$$\mathbf{q}_{N_s(n) \times 1}^{(b,n)} = \mathbf{C}_{N_s(n) \times N}^{(n)} \mathbf{W}_{N \times 1}^{(k_0)}. \quad (12)$$

IV. LOOK-UP TABLE BASED DFT-S-OFDM-F IMPLEMENTATION

For basic LUT-based DFT-s-OFDM-F, the structure of Fig. 1 is used for generating the LUT contents separately for each of the B input symbols of a block. During on-line processing, the sample vectors corresponding to the actual input symbols are fetched from the LUT and added up. The following subsections first show the basic idea of LUT-OFDM, then the different variants of LUT-OFDM are introduced. The computational complexity and memory requirements of the different LUT-OFDM variants are analyzed in Appendix A.

A. Basic input symbol based processing

We assume that the low-rate input data symbols $a_{b,n}$ in (1) are QPSK, BPSK, $\pi/4$ -QPSK, or $\pi/2$ -BPSK symbols. Hence, $a_{b,n}$ can be expressed as

$$a_{b,n} = \begin{cases} \left(\frac{1+j}{\sqrt{2}} \right) (-j)^{d_{b,n}}, & \text{for QPSK} \\ \left(\frac{1+j}{\sqrt{2}} \right) (-1)^{d_{b,n}}, & \text{for BPSK} \\ \left(\frac{1+j}{\sqrt{2}} \right)^{\langle n \rangle_{2+1}} (-j)^{d_{b,n}}, & \text{for } \pi/4\text{-QPSK} \\ j^{\langle n \rangle_{2}} \left(\frac{1+j}{\sqrt{2}} \right) (-1)^{d_{b,n}}, & \text{for } \pi/2\text{-BPSK}, \end{cases} \quad (13)$$

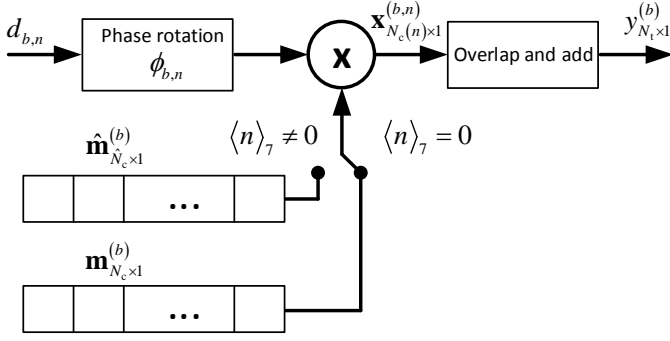


Fig. 2. Basic LUT-OFDM for the normal CP configuration of LTE with BPSK or QPSK modulation. The block diagram shows the processing for the b th input symbol. Here, $\hat{\mathbf{m}}_{N_c \times 1}^{(b)}$ and $\mathbf{m}_{N_c \times 1}^{(b)}$ stand for the stored data for the first symbol and for the rest of symbols in a slot, respectively.

where $d_{b,n}$ represents the mapping of the data symbols, with $d_{b,n} = [0, 1, \dots, D-1]$, $D = 4$ for QPSK and $\pi/4$ -QPSK modulations, and $D = 2$ for BPSK and $\pi/2$ -BPSK.¹ Here $a_{b,n}$ contains some multiplicative elements which are independent of the symbol value $d_{b,n}$, i.e., $(1+j)/\sqrt{2}$ for BPSK and QPSK, $((1+j)/\sqrt{2})^{\langle n \rangle_2 + 1}$ for $\pi/4$ -QPSK, and $j^{\langle n \rangle_2}((1+j)/\sqrt{2})$ for $\pi/2$ -BPSK. These elements can be combined with the DFT-s-OFDM-F processing vector as follows:

$$\mathbf{m}_{N_c(n) \times 1}^{(b,n)} = \begin{cases} \left(\frac{1+j}{\sqrt{2}} \right) \mathbf{f}_{N_c(n) \times 1}^{(b,n)}, & \text{for BPSK \& QPSK} \\ \left(\frac{1+j}{\sqrt{2}} \right)^{\langle n \rangle_2 + 1} \mathbf{f}_{N_c(n) \times 1}^{(b,n)}, & \text{for } \pi/4\text{-QPSK} \\ j^{\langle n \rangle_2} \left(\frac{1+j}{\sqrt{2}} \right) \mathbf{f}_{N_c(n) \times 1}^{(b,n)}, & \text{for } \pi/2\text{-BPSK.} \end{cases} \quad (14)$$

As a result, it is possible to compute (14) and store the precomputed DFT-s-OFDM-F symbols in a look-up table. In other words, $\mathbf{m}_{N_c(n) \times 1}^{(b,n)}$ contains all necessary processing for DFT-s-OFDM-F such as DFT, IFFT, and filtering, which can be computed once and stored in the device memory, leaving only trivial phase rotations to be done in real-time. The stored data is multiplied by the phase rotation of $\phi_{b,n} = (-1)^{d_{b,n}}$ for BPSK and $\pi/2$ -BPSK, or $\phi_{b,n} = (-j)^{d_{b,n}}$ for QPSK and $\pi/4$ -QPSK. As a result, the DFT-s-OFDM-F block due to single subcarrier in (1) can be reformulated as follows:

$$\mathbf{x}_{N_c(n) \times 1}^{(b,n)} = \mathbf{m}_{N_c(n) \times 1}^{(b,n)} \phi_{b,n}. \quad (15)$$

Consequently, the subcarrier overlap-and-add process in (7) is applied, resulting in DFT-s-OFDM-F structure without multiplications. The aforementioned process is represented in Fig. 2 for the BPSK and QPSK cases, showing the basic LUT scheme with overlap-and-add process to obtain the DFT-s-OFDM-F waveform.

For the normal CP configuration, equal CP length is assigned for the symbols in a slot except for the first symbol, leading to two different lengths of the DFT-s-OFDM-F symbols: one for the first symbol and the other for the rest of the symbols. Thus, for BPSK and QPSK, the stored data

¹These symbol values follow the NB-IoT specifications, but also other definitions of the basic constellations can be treated in the same way.

0	0	0	0	0	0	0	0	0	0	0	0	0	0	0	0	0
0	0	0	0	1	1	1	1	2	2	2	2	3	3	3	3	
0	1	2	3	0	1	2	3	0	1	2	3	0	1	2	3	

Fig. 3. Example of the alternativity matrix $\mathbf{J}_{G \times P}$ for QPSK with $D = 4$, $G = 3$, and assuming that the first symbol is fixed to $d_{0,r,n} = 0$. The number of needed possibilities is $P = 16$.

consists of B different sample vectors $\hat{\mathbf{m}}_{N_c \times 1}^{(b)}$ for the first DFT-s-OFDM-F symbol with $\langle n \rangle_7 = 0$, and additional B different sample vectors $\mathbf{m}_{N_c \times 1}^{(b)}$ for the other symbols of a slot with $\langle n \rangle_7 \neq 0$. Then the total number of sample vectors for LUT processing is $2B$. The lengths of these sample vectors are $\hat{N}_c = \hat{N}_s + N_h - 1$ and $N_c = N_s + N_h - 1$, respectively. Regarding the extended CP configuration of LTE, all CP lengths of a slot are equal and B sample vectors are enough.

Eq. (14) contains an additional symbol index dependent phase rotation for both $\pi/2$ -BPSK and $\pi/4$ -QPSK. For $\pi/2$ -BPSK, the phase rotation is a trivial multiplication that can be applied without the need to store different vectors for even and odd symbols, by slightly modifying the logic of the "phase rotation" block in Fig. 2. For $\pi/4$ -QPSK, separate LUTs are needed for even and odd DFT-s-OFDM-F symbol indices in order to handle the multiplication of even symbols by $(1+j)/\sqrt{2}$ in a multiplier-free way.

B. Input symbol grouping

The computational complexity (i.e., the number of additions) of LUT-OFDM can be reduced by processing the input symbols group-wise [21], [22]. Then the partial waveforms corresponding to all possible combinations of $d_{b,n}$ in the group are stored. Without loss of generality, we assume that the B input symbols are divided into R groups of equal size with $G = B/R$ symbols in each. Let $r \in \{0, 1, \dots, R-1\}$ and $g \in \{0, 1, \dots, G-1\}$ denote the group index and symbol index within each group, respectively. While the indices g and r can be assigned in an arbitrary way for the allocated subcarriers, we can assume that symbols with indices $b = \{0, 1, \dots, R-1\}$ are in group 1 with $g = b$, symbols with indices $b = \{R, R+1, \dots, 2R-1\}$ are in group 2 with $g = b-R$, etc. The number of alternative symbol combinations in each group is D^G .

Each possible combination of input symbols takes an address index $p \in \{0, 1, \dots, P-1\}$, and it should be placed in the memory in such a way that the address index p can be decomposed to the following form

$$p = d_{0,r,n} D^{G-1} + d_{1,r,n} D^{G-2} + \dots + d_{G-1,r,n}, \quad (16)$$

where $d_{g,r,n} \in \{0, 1, \dots, D-1\}$ denotes the g th input symbol of group r . The possible symbol mappings can be arranged in ascending way as

$$(\mathbf{J}_{G \times P})_{(g+1)(p+1)} = \left\langle \left\lfloor \frac{p}{D^{G-(g+1)}} \right\rfloor \right\rangle_D, \quad (17)$$

where $g+1$ and $p+1$ are the matrix row and column indices, respectively. An example construction of the alternativity matrix $\mathbf{J}_{G \times P}$ with $G = 3$ and $D = 4$ is illustrated in Fig. 3. It can be noted that the elements of $\mathbf{J}_{G \times P}$ are similar to counting in the

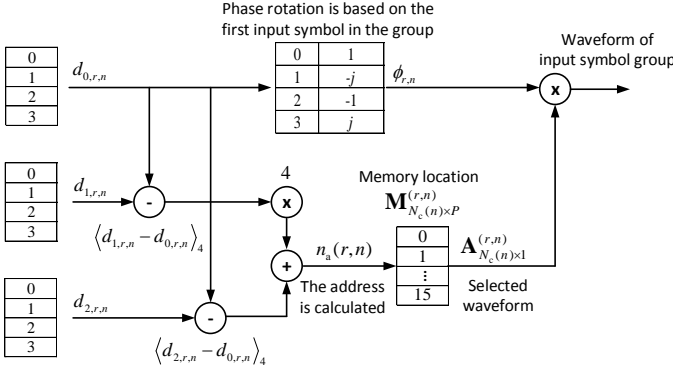


Fig. 4. Example of waveform construction and data allocation of the input symbol grouping based LUT using QPSK, $G = 3$ and the number of alternatives is $P = 16$ for the r th group.

base- D numerals. The alternativity matrix helps to construct the stored sample matrix per group as

$$\mathbf{M}_{N_c(n) \times P}^{(r,n)} = \begin{cases} \mathbf{F}_{N_c(n) \times G}^{(r,n)} (-j)^{\circ \mathbf{J}_{G \times P}}, & \text{for QPSK} \\ \mathbf{F}_{N_c(n) \times G}^{(r,n)} (-1)^{\circ \mathbf{J}_{G \times P}}, & \text{for BPSK,} \end{cases} \quad (18)$$

where $\mathbf{F}_{N_c(n) \times G}^{(r,n)}$ is a matrix constructed as

$$\mathbf{F}_{N_c(n) \times G}^{(r,n)} = \begin{bmatrix} \mathbf{f}_{N_c(n) \times 1}^{(0,r,n)} & \mathbf{f}_{N_c(n) \times 1}^{(1,r,n)} & \dots & \mathbf{f}_{N_c(n) \times 1}^{(G-1,r,n)} \end{bmatrix}, \quad (19)$$

and $\mathbf{f}_{N_c(n) \times 1}^{(g,r,n)}$ is equivalent to the DFT-s-OFDM-F processing vector in (2) with appropriate mapping of the symbol index b , e.g., $g = \langle b \rangle_G$ and $r = \lfloor b/G \rfloor$.

We can exploit phase rotations to reduce the number of alternatives to $P = D^{G-1}$. This can be achieved by normalizing the first input symbol of each group in the LUT to the constant value of 0, corresponding to zero phase rotation, and applying a proper phase rotation to the LUT output according to the actual first input symbol value. The needed rotation is $\phi_{r,n} = (-1)^{d_{0,r,n}}$ or $(-j)^{d_{0,r,n}}$ for BPSK or QPSK, respectively. Then the LUT addressing logic is modified in such a way that the needed phase rotation results in correct output also for the other input symbols. This means that the LUT output should be selected according to the symbol combination with $\langle d_{g,r,n} - d_{0,r,n} \rangle_D$ for $g = 1, 2, \dots, G-1$. This is achieved by using the following address for the stored data:

$$\begin{aligned} n_a(r,n) = & \langle d_{1,r,n} - d_{0,r,n} \rangle_D D^{G-2} \\ & + \langle d_{2,r,n} - d_{0,r,n} \rangle_D D^{G-3} \\ & + \dots + \langle d_{G-1,r,n} - d_{0,r,n} \rangle_D. \end{aligned} \quad (20)$$

The input symbol grouping and fetching the waveform from the memory address is shown in Fig. 4. Finally, the waveform of the DFT-s-OFDM-F subframe per group can be calculated as

$$\mathbf{y}_{N_t \times 1}^{(r)} = \sum_{n=0}^{N_t-1} \phi_{r,n} \mathbf{S}_{N_t \times N_c(n)}^{(n)} \mathbf{A}_{N_c(n) \times 1}^{(r,n)}, \quad (21)$$

where $\mathbf{A}_{N_c(n) \times 1}^{(r,n)}$ is the $(n_a(r,n) + 1)$ th column of the stored sample matrix $\mathbf{M}_{N_c(n) \times P}^{(r,n)}$. Here, the output waveform is rep-

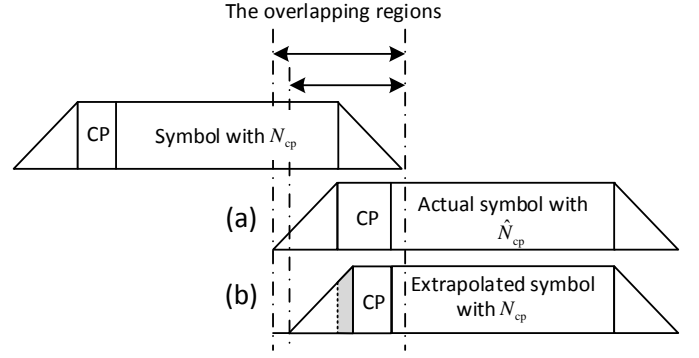


Fig. 5. Illustration of the overlapping with (a) long CP and (b) extrapolated CP.

resented per group. Accordingly, the total output is the sum over all symbol groups $r = 0, 1, \dots, R-1$.

In normal CP configuration, the stored data consists of R different sample matrices for the first symbol of the slot when $\langle n \rangle_7 = 0$ and additional R different sample matrices for the rest of the symbol in the slot when $\langle n \rangle_7 \neq 0$. In case of equal CP lengths in the subframe (like extended CP configuration of LTE), the stored data contains R different sample matrices, which are common for all symbols.

C. CP extrapolation

In the LUT scheme presented above, the memory size is doubled in the normal CP configuration due to the difference of the CP lengths within the slot. However, it is possible to save half of this memory by generating the filtered DFT-s-OFDM-F symbols for different CP lengths from the same stored sample vectors or matrices. Our idea is to extrapolate the additional sample(s) for the first (longer) CP from the sample vector or matrix created for the shorter length. Notably, with LTE numerology and the minimum IFFT length² of $N = 128$, just one additional sample is needed for the first DFT-s-OFDM-F symbol. The simplest way for extrapolation is to insert zero-valued samples in front of the first CP as a guard period, and let the filtering process do the extrapolation. This is equivalent to using the same sample vector as for shorter CPs, but reducing the overlap with the previous sample vector in the beginning (by one sample when $N = 128$). It was verified by simulations that the effect of this approach on the link performance is insignificant. Fig. 5 shows the overlapping process for the normal CP configuration, illustrating the CP extrapolation idea. Accordingly, the modification applies on the CP matrix of the first symbol in the slot as follows:

$$\hat{\mathbf{C}}_{\hat{N}_s \times N} = \begin{bmatrix} \mathbf{0}_{(\hat{N}_{cp} - N_{cp}) \times N} \\ \mathbf{0}_{N_{cp} \times (N - N_{cp})} \quad \mathbf{I}_{N_{cp}} \\ \mathbf{I}_N \end{bmatrix}. \quad (22)$$

Therefore, the extended DFT-s-OFDM-F symbol is equivalent to other DFT-s-OFDM-F symbols except for $(\hat{N}_{cp} - N_{cp})$ zeros at the beginning of the extended symbol. Accordingly, the stored data consists of B/G sample matrices $\mathbf{M}_{N_c \times P}^{(r)}$ that is calculated according to (18) for all values of n .

²For smaller N , the CP length is not an integer anymore.

D. Storing the symbol transitions

The number of additions of the LUT scheme can be reduced even further by storing all possible filtered transition intervals between DFT-s-OFDM-F symbols in (21). This can be done by considering all alternative combinations of consecutive symbols. The used approach here for waveform creation and storage is similar to the input symbol grouping, including also the use of multiples of $\pi/2$ radian phase rotations to save some memory space. The non-overlapping center parts of the DFT-s-OFDM-F symbols are obtained according to (18), and the address is obtained according to (20). The filtered transitions between symbols are generated as follows. The number of alternatives for filter transitions is computed as $P' = D^{2G-1}$. The addressing index of $p' \in \{0, 1, \dots, P' - 1\}$ for filter transitions should be decomposed as

$$p' = d_0 D^{2G-1} + d_1 D^{2G-2} + \dots + d_{2G-1}, \quad (23)$$

where $d_0, d_1, \dots, d_{2G-1}$ are the possible mappings of the g' th input symbol in the group, where $g' \in \{0, 1, \dots, 2G - 1\}$. The input symbols of a group of the prior DFT-s-OFDM-F symbol n are represented by the data symbol mapping of d_0, d_1, \dots, d_{G-1} , whereas the input symbols of the corresponding group of the later symbol $n + 1$ are represented by $d_G, d_{G+1}, \dots, d_{2G-1}$. Each data symbol mapping takes values from $\{0, 1, \dots, D - 1\}$ except for $d_0 = 0$. Consequently, the transition alternativality matrix is created in similar way as (17) with the new dimensions, i.e., $\mathbf{J}_{2G \times P'}$. Then the stored tail-sample matrix per input symbol group can be computed as

$$\mathbf{M}_{N_c(n) \times P'}^{(r,n)} = \begin{cases} \mathbf{T}_{N_T(n) \times 2G}^{(r,n)} (-j)^{\circ \mathbf{J}_{2G \times P'}}, & \text{for QPSK} \\ \mathbf{T}_{N_T(n) \times 2G}^{(r,n)} (-1)^{\circ \mathbf{J}_{2G \times P'}}, & \text{for BPSK,} \end{cases} \quad (24)$$

where $N_T(n) = N_h - (N_{cp}(n) - N_{cp}) - 1$, and $\mathbf{T}_{N_T(n) \times 2G}^{(r,n)}$ is constructed as

$$\mathbf{T}_{N_T(n) \times 2G}^{(r,n)} = \begin{bmatrix} \mathbf{f}_{N_T(n) \times 1}^{(0,r,n)} & \mathbf{f}_{N_T(n) \times 1}^{(1,r,n)} & \dots & \mathbf{f}_{N_T(n) \times 1}^{(G-1,r,n)} \\ \mathbf{f}_{N_T(n+1) \times 1}^{(0,r,n+1)} & \mathbf{f}_{N_T(n+1) \times 1}^{(1,r,n+1)} & \dots & \mathbf{f}_{N_T(n+1) \times 1}^{(G-1,r,n+1)} \end{bmatrix}, \quad (25)$$

where $\mathbf{f}_{N_T(n) \times 1}^{(g,r,n)}$ is the last $N_T(n)$ samples of $\mathbf{f}_{N_c(n) \times 1}^{(g,r,n)}$ and $\mathbf{f}_{N_T(n+1) \times 1}^{(g,r,n+1)}$ is the first $N_T(n+1)$ samples of $\mathbf{f}_{N_c(n+1) \times 1}^{(g,r,n+1)}$. Then the phase rotation is calculated using data symbol mapping of value $d_{0,r,n}$. The address index can be computed as follows:

$$n'_a(r,n) = \langle d_{1,r,n} - d_{0,r,n} \rangle_D D^{2G-2} + \dots + \langle d_{G-1,r,n} - d_{0,r,n} \rangle_D D^G + \langle d_{0,r,n+1} - d_{0,r,n} \rangle_D D^{G-1} + \dots + \langle d_{G-1,r,n+1} - d_{0,r,n} \rangle_D. \quad (26)$$

Finally, the LUT-OFDM can be created by obtaining the corresponding data from the address, followed by the trivial phase rotation. If $G < B$, the transitions of the corresponding input symbol groups are added up.

Fig. 6 shows different cases of overlapping and non-overlapping regions of transmitted symbols, which are subjected to the transition storing process and input symbol grouping process (possibly with extrapolation), respectively. Overlapping region 2 represents slot boundaries, whereas

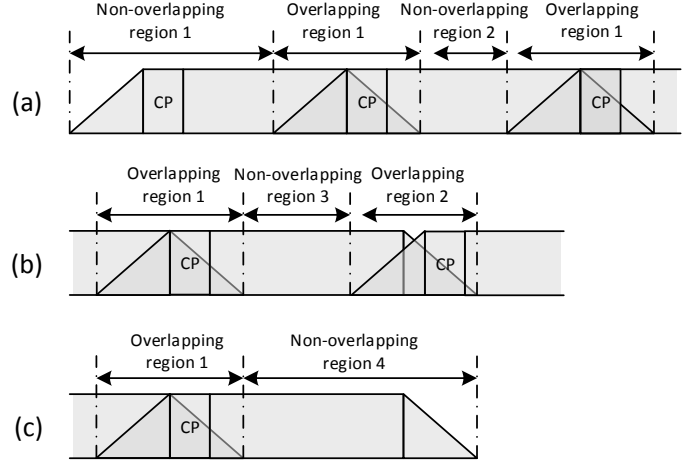


Fig. 6. Illustration of non-overlapping and overlapping samples at the (a) beginning, (b) middle, and (c) end of the transmitted symbols.

overlapping region 1 represents all other symbol boundaries within a slot. Accordingly, the stored data contains two sets of B/G different tail-sample matrices $\mathbf{M}_{N_c(n) \times P'}^{(r,n)}$, one for each overlapping region type. Non-overlapping region 1 represents the non-overlapping part at the beginning of the transmission. Non-overlapping regions 2 and 3 are the non-overlapped parts at the middle of the transmission while region 4 shows the non-overlapped part at the end of the transmission. The stored data consists of B/G different matrices $\mathbf{M}_{N_c \times P}^{(r)}$ which are sufficient for the implementation of all the non-overlapping regions.

E. LUT-based WOLA

The main idea of windowed overlap and add (WOLA) [13] is to enhance the spectrum containment of CP-OFDM or DFT-s-OFDM by using smooth transitions between consecutive OFDM symbols, instead of the rectangular window of the basic CP-OFDM scheme. This is done by including both cyclic prefix and cyclic postfix around the OFDM symbol and shaping the resulting extended symbol by a smooth window function. Typically, a raised-cosine function is used for this purpose in such a way that the window tapers are outside the main OFDM symbol and effective part of the CP. The leading taper of an OFDM symbol usually overlaps with the tailing taper of the previous one. WOLA has very low implementation complexity, but it tends to increase the intersymbol interference unless the channel delay spread is small compared to the CP length. WOLA based OFDM and DFT-s-OFDM waveforms can be generated in the same way as the corresponding filtered waveforms, just using window processing instead of filtering when generating the LUT contents.

F. System specific aspects

Above the NB-IoT and LTE specific parameters were considered for simplicity of discussion. However, the ideas can be easily generalized, e.g., in the following respects:

- Arbitrary rotations of basic BPSK and QPSK constellations can be used instead of the $\pi/4$ -rotated ones in (13).

Obviously, the LUT size grows quickly if higher-order constellations are considered.

- Without frequency shift by half subcarrier spacing, i.e., removing the latter term in (5).
- CP extrapolation can be used with different schemes of variable CP lengths, as long as the variations are relatively small.

Concerning the NB-IoT application, one further element of 3GPP specifications need to be considered in the single-tone case. The basic OFDM and DFT-s-OFDM generation models align the phase at the beginning of the useful part of the OFDM symbol to follow the phase of the modulating data value. Consequently, the phase at the beginning of the CP part depends on the CP length and the subcarrier frequency. Also the phase transition between consecutive OFDM symbols is affected. The purpose of phase rotations in $\pi/2$ -BPSK and $\pi/4$ -QPSK is to have controlled and reduced phase transitions between symbols. Therefore, NB-IoT has adopted so-called phase alignment model for single-tone uplink transmission. The modulating phase values are adjusted for each symbol in such a way that the phase transitions exactly follow those used for $\pi/2$ -BPSK or $\pi/4$ -QPSK scheme [25]. The needed additional phase rotation accumulates over the subframe, with the periodicity of four slots when the half-subcarrier frequency shift is included. However, the phase rotation between consecutive slots is $\pm\pi/2$, which can be achieved by trivial phase rotations of stored sample vectors. With the normal CP-based LTE slot structure, all the seven OFDM symbols of a slot need their own LUTs, which increases the total LUT size for single-tone allocations considerably.

Another, more generic aspect is that a device usually needs the capability to support different allocations with different numbers of subcarriers and different center frequencies. The most straightforward approach is to store separate LUTs for all needed allocations. It may be possible to utilize conjugate symmetry to reduce the number of LUTs, but the spreading transform of DFT-s-OFDM complicates this approach. With NB-IoT specifications, conjugate symmetry can be used only in the single-tone case, to reduce the number of LUTs to six for the 12 alternative allocations. Alternatively, utilizing the given expressions, it is possible to recalculate effectively random access memory (RAM)-based LUT contents whenever the parameters are changed. If the downlink transmission capacity is sufficient, the recalculation could also be performed at the base station side, which allows the network operators to control directly the signal quality and other parameters of low-cost IoT devices.

V. NUMERICAL RESULTS

We start this section by showing the effects of spectrum enhancement on the coexistence of LTE and NB-IoT. Then we evaluate the computational complexity and memory requirements of LUT-OFDM and compare the results with conventional schemes. Moreover, in this section we test the performance of the LUT-OFDM schemes in finite-wordlength scenarios while showing the in-band emission, out-of-band emission, and error-vector magnitude (EVM) of the quantized

LUT-OFDM signals. Consequently, the minimum wordlength requirements for reaching the 3GPP specification [10] are provided. These metrics are revisited when using practical power amplifier (PA) with the quantized LUT-OFDM waveforms.

A. Spectrum enhancement for LTE and NB-IoT coexistence

Here we consider NB-IoT deployment in the guard-band of a 10 MHz LTE carrier based on full link-level simulations using the Matlab LTE-toolbox. We assume 45 kHz (three subcarriers) guard-band between the active subcarriers of LTE and NB-IoT. Asynchronous operation is modeled by a relative timing offset of quarter of the OFDM symbol duration. Considering power control imperfections, we define the ideal reference case based on the signal-to-noise ratios (SNRs) needed under interference-free conditions to reach 10 % block error-rate (BLER) for LTE and NB-IoT systems. The obtained SNR difference defines the optimal power difference of the two signals at the base-station receiver, i.e., the operation point if there would be no inter-system-interference.

We examine first the interference from asynchronous twelve-tone NB-IoT to a single-PRB LTE allocation considering four different modulation and coding schemes (MCSs) for LTE: 64-QAM subcarrier modulation and code rate of $R = 5/6$, 16-QAM with $R = 2/3$, QPSK with $R = 2/3$, and QPSK with $R = 1/3$. NB-IoT is assumed to use QPSK modulation and code rate of $R = 2/3$ in all cases. Further, 10 dB power offset is assumed such that the NB-IoT power is 10 dB stronger than in the reference case. As an example, LTE with 64-QAM modulation and $R = 5/6$ is 14.0 dB stronger than NB-IoT with $R = 2/3$ in the reference case. In the test case with 10 dB power offset, LTE is 4.0 dB stronger than NB-IoT at the base-station receiver.

The results are shown in Fig. 7 for additive white Gaussian noise (AWGN) channel without any filtering or windowing, as well as with filtering in the NB-IoT transmitter (Tx) and/or LTE receiver (Rx). LTE and NB-IoT systems run with sampling rates of 15.36 MHz and 1.92 MHz, and use raised-cosine filters of length 480 samples and 60 samples, respectively. We can see that in this test case, guard-band NB-IoT causes significant degradation to the LTE link performance. Filtering at the NB-IoT Tx significantly reduces the interference leakage, and so does the filtering at the LTE Rx. By including filtering on both sides, essentially interference-free link performance is achieved. Without any spectrum enhancement, the performance loss at 1 % BLER level is about 1.5 dB in all considered cases. In the reference cases without power offset, some minor benefit (in the order of 0.15 dB) from spectrum enhancement can be observed. Regarding the case where NB-IoT uses QPSK with $R = 1/3$ with 10 dB power offset, the LTE performance loss was found to be clearly smaller, about 0.4 dB in the 16-QAM and 64-QAM cases. However, with 15 dB power offset, NB-IoT with $R = 1/3$ reaches similar relative power levels as NB-IoT with $R = 2/3$ and 10 dB power offset, introducing about 1.5 dB performance loss for LTE.

Fig. 8 shows the NB-IoT link performance as a victim of interference from the LTE system in the same scenario,

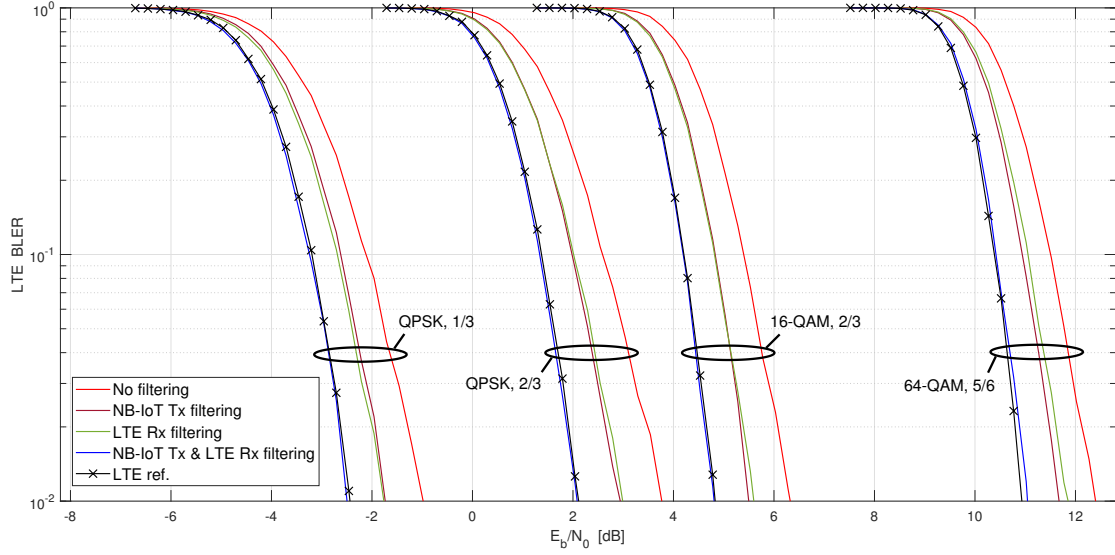


Fig. 7. Examples of filtering effects on LTE uplink performance with different modulation and coding schemes in the presence of asynchronous NB-IoT guard-band deployment. NB-IoT uses QPSK modulation with code rate 2/3 and its signal power is 10 dB stronger than in the reference case.

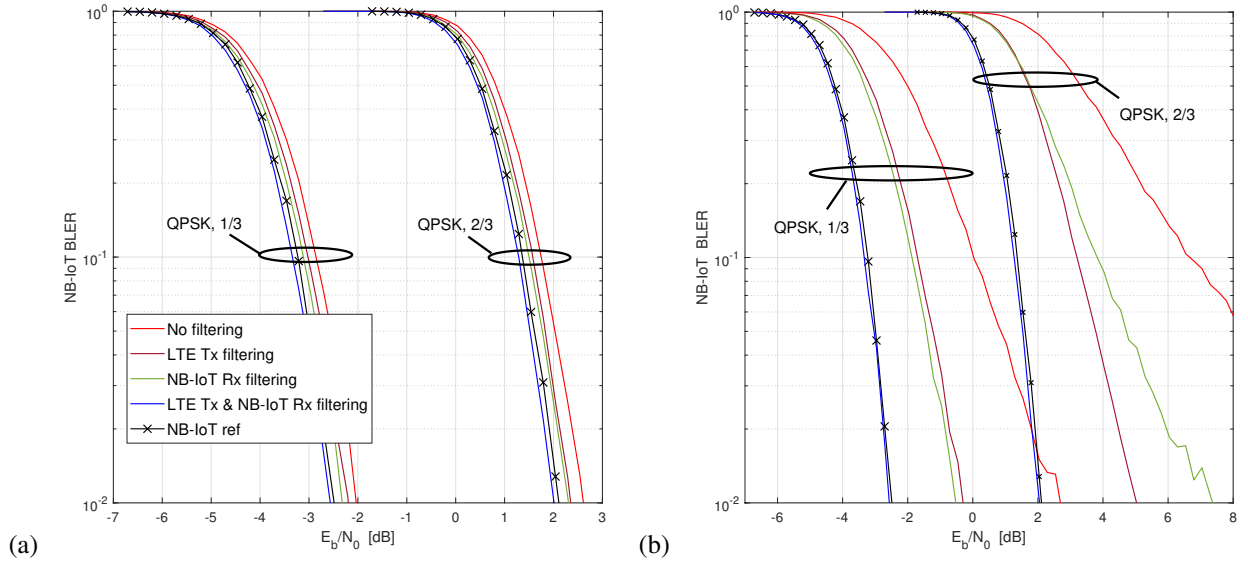


Fig. 8. Examples of filtering effects on asynchronous NB-IoT uplink performance in guardband deployment. NB-IoT uses QPSK modulation and code rates 1/3 and 2/3. Reference power control case without power offset. (a) LTE uses 16-QAM with code rate 2/3. (b) LTE uses 64-QAM with code rate 5/6.

considering LTE with 64-QAM with $R = 5/6$ and 16-QAM with $R = 2/3$. Here NB-IoT uses QPSK modulation with $R = 1/3$ or $R = 2/3$ and the results are for the reference cases without power offset. With high MCS, LTE without spectrum enhancement causes severe interference to NB-IoT operation. The performance loss at 1 % BLER level is 5 dB or more in the 64-QAM cases and about 0.5 dB in the 16-QAM cases. For LTE with QPSK, the loss is rather small, 0.4-0.5 dB. Again, filtering mitigates the interference leakage effectively and when applied at both LTE Tx and NB-IoT Rx, NB-IoT reaches similar performance as in the interference-free cases.

In all considered test scenarios, the LTE and NB-IoT systems with both Tx and Rx filtering reach the performance of the corresponding basic DFT-s-OFDM reference schemes

without filtering and operating under interference-free conditions.

Even though the NB-IoT and LTE would ideally operate synchronously in the guard-band NB-IoT deployment, these results indicate the possibility to relax the synchronization and power control requirements. This is especially important in possible deployments of NB-IoT within a 5G-NR carrier, in which case inter-numerology interference is a critical issue, demanding spectrum enhancement also in mMTC devices.

B. Implementation complexity

Here we compare the memory requirements and computational complexity of different DFT-s-OFDM-F transmission schemes. A detailed analysis can be found in Appendix A. The

complexity of DFT-s-OFDM without filtering or windowing is used as a basic reference in all evaluated cases. The spectrally enhanced non-LUT DFT-s-OFDM schemes include the WOLA-scheme (DFT-s-OFDM-W), time-domain filtering scheme (DFT-s-OFDM-F), the fast-convolution scheme (DFT-s-OFDM-FC), and the narrowband decomposed FC scheme (DFT-s-OFDM-NB-D-FC) [19]. The LUT-based schemes include WOLA based (LUT-W) and filtering based (LUT-F) ones, with prefix E for CP extrapolation and TS for transition storing (i.e., TS-LUT-W stands for WOLA-based LUT scheme with transition storing and extrapolation). These schemes are tested using the transform size of $N = 128$, which is the smallest size with integer CP lengths. The CP lengths are 10 and 9 samples for normal CP mode. Moreover, the $\pi/2$ -BPSK and $\pi/4$ -QPSK are used only for single-tone cases, while binary phase shift keying (BPSK) and quadrature phase shift keying (QPSK) are considered for multi-tone cases. Filter lengths of 33 and 120 are considered as extreme cases when searching for suitable performance vs. complexity trade-off. In WOLA cases we use raised-cosine windows with five nontrivial samples per window taper (i.e., about half of the CP length). FC-based schemes contain three transforms of size 128, one used as OFDM transform and the other two for the FC filtering process [18]. In DFT-s-OFDM-NB-D-FC, the last one is decomposed according to the number of active subcarriers [19].

Firstly, we focus on the coefficient memory requirements of different schemes. This is expressed in terms of memory words required for the real and imaginary parts of the coefficients of the non-LUT schemes and waveform samples in the LUT schemes. The coefficient wordlength requirements will be discussed later in this section.

The required memory for the coefficients of the non-LUT schemes are 61 memory units for DFT-s-OFDM, 71 memory units with WOLA processing, 63 memory units for FC-based schemes, and 160 or 421 memory units for DFT-s-OFDM-F with filter lengths of 33 or 120, respectively. These memory calculations comprise the permanent memory requirements for split-radix IFFT implementation of size 128. Moreover, it comprises the frequency-domain masking for FC-based schemes or time-domain filtering for DFT-s-OFDM-F scheme.

Table II shows the memory requirements for the different variants of filtering based LUT-OFDM with different allocation bandwidths and grouping arrangements using BPSK and QPSK in normal CP configurations with filter lengths of 33 and 120. Here fixed allocations without phase alignment are assumed. The basic scheme, with different LUTs for different CP lengths, is excluded from the table because the required memory is doubled with respect to the CP extrapolation case, while it was verified that the differences in link performance are marginal. The table shows significant differences in the memory usage between QPSK and BPSK. Moreover, the group size affects the memory requirements greatly. Transition storing is useful mainly with group size of one and group size of three for binary modulation. Groups of 12 are completely unrealistic, while the group size of 6 might be considered feasible only with binary modulation.

Table III shows the total memory requirements for LUT-

TABLE II
PER ALLOCATION MEMORY REQUIREMENTS IN REAL SAMPLES FOR DIFFERENT FILTERING-BASED LUT-OFDM VARIANTS IN NORMAL CP CONFIGURATION OF LTE WITH $N = 128$ AND WITHOUT PHASE ALIGNMENT. THE UPPER AND LOWER NUMBERS REPRESENT FILTER LENGTHS OF $N_h = \{33, 120\}$, RESPECTIVELY. THE MEMORY SIZES IN BOLD ARE CONSIDERED POTENTIALLY USEFUL IN PRACTICE.

Subband size	Group size	Extrapolation		Transition storing	
		BPSK	QPSK	BPSK	QPSK
1	1	338	676	590	1684
		512	1024	1460	4816
3	1	1014	1014	1770	2526
		1536	1536	4380	7224
	3	1352	5408	5384	134432
		2048	8192	17216	493568
6	1	2028	2028	3450	5052
		3072	3072	8760	14448
	3	2704	10816	10768	268864
		4096	16384	34432	987136
	6	10816	346112	268864	0.5×10^9
		16384	524288	987136	2.0×10^9
12	1	4056	4056	7080	10104
		6144	6144	17520	28896
	3	5408	21632	21536	537728
		8192	32768	68864	2.0×10^6
	6	21632	692224	537728	1.1×10^9
		32768	1.0×10^6	2.0×10^6	4.0×10^9
	12	692224	1.4×10^9	1.1×10^9	8.9×10^{15}
		1.0×10^6	2.1×10^9	4.0×10^9	0.3×10^{18}

OFDM based transmitter of a NB-IoT device. Here also the WOLA-based LUT schemes are included, showing only approximately 13 % lower complexity than the short filter ($N_h = 33$) based LUT-OFDM. Based on [10], not all possible mixtures of single-, three-, and six-tone allocations are considered in practical operation. Here four three-tone allocations with subcarrier sets $\{-6, -5, -4\}$, $\{-3, -2, -1\}$, $\{0, 1, 2\}$, and $\{3, 4, 5\}$ are included. Two six-tone allocations with subcarrier sets $\{-6, -5, -4, -3, -2, -1\}$ and $\{0, 1, 2, 3, 4, 5\}$ are included. In single-tone cases, there are 12 possible allocations, but conjugate symmetry is applied to reduce the number of LUTs to 6 sets of 7 LUTs, with separate LUTs for each symbol within a slot to support phase alignment. For simplicity, only single input symbol processing with CP extrapolation is used, i.e., input symbol grouping and transition storing schemes are not considered in Table III. In this table, also the non-phase-aligned cases are included for single-tone transmission, highlighting the increased memory requirements due to the phase alignment of the 3GPP specifications and *promoting the need for a modified specification in 5G-NR and beyond for more efficient LUT based implementation*.

Secondly, the normalized rates of real multiplications and additions per QPSK or BPSK symbol with the filter lengths

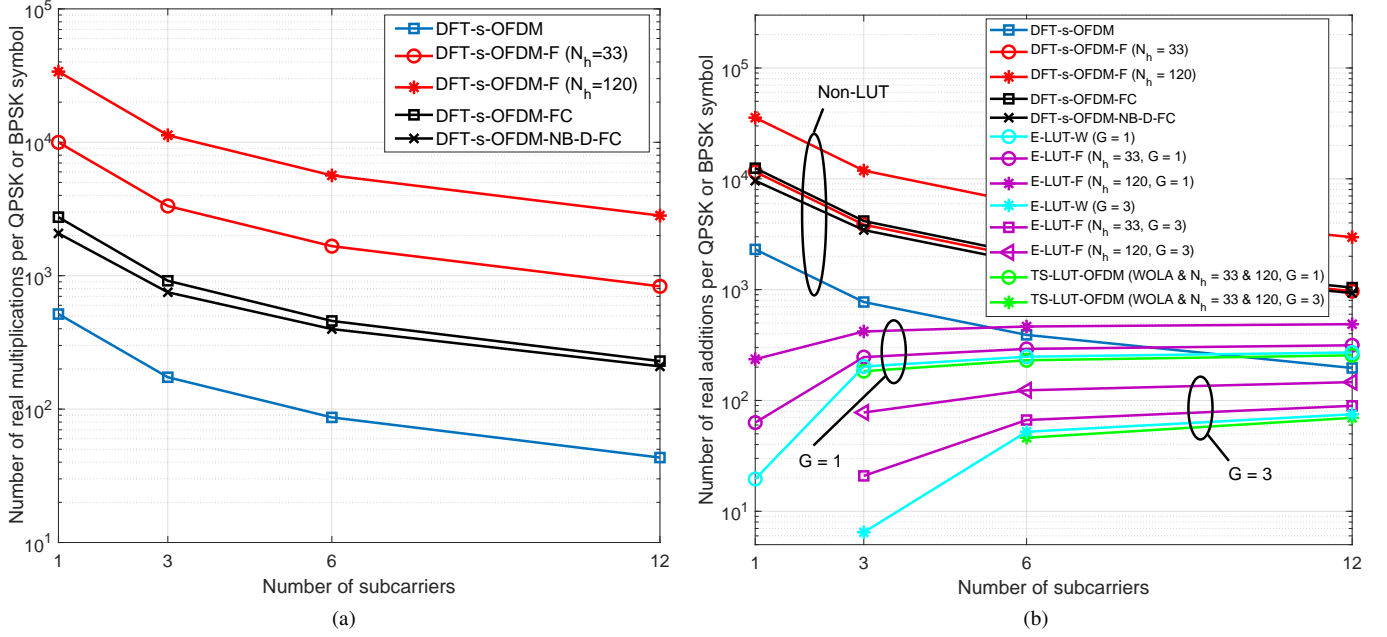


Fig. 9. (a) Real multiplication rates and (b) real addition rates per transmitted QPSK or BPSK symbol for different DFT-s-OFDM schemes. The real multiplication rates of the LUT-OFDM schemes are not shown because they are zero for all configurations. The transition-storing curves of addition rates start from zero. However, these values are not shown due to the logarithmic y-scale.

TABLE III

TOTAL MEMORY REQUIREMENTS IN REAL SAMPLES FOR LUT-OFDM BASED NB-IoT DEVICE WITH $N = 128$ WITH AND WITHOUT PHASE ALIGNMENT. THE UPPER NUMBERS REPRESENT WOLA-BASED LUT AND THE MIDDLE AND LOWER NUMBERS REPRESENT FILTER LENGTHS OF $N_h = \{33, 120\}$, RESPECTIVELY.

Subband size	Possible allocations	Per subcarrier allocation		All subcarrier allocations	
		BPSK	QPSK	Without phase alignment	With alignment
1	12	294	588	5292	37044
		338	676	6084	42588
		512	1024	9216	64512
3	4	–	882	3528	3528
		–	1014	4056	4056
		–	1536	6144	6144
6	2	–	1764	3528	3528
		–	2028	4056	4056
		–	3072	6144	6144
12	1	–	3528	3528	3528
		–	4056	4056	4056
		–	6144	6144	6144
				15876	47628
All allocations				18252	54756
				27648	82944

of 33 and 120 are shown in Fig. 9.

In Fig. 9(a), it can be seen that the time-domain filtering scheme (DFT-s-OFDM-F) needs significantly higher multipli-

cation rates compared with the FC based schemes.³ Regarding the addition rates shown in Fig. 9(b), the unrealistic cases of group sizes 6 and 12 are avoided. Moreover, the basic LUT case for variable CP lengths is not shown since it has significantly higher memory requirement and complexity compared with the extrapolated case. *Generally, it can be seen that LUT-OFDM variants reach lower addition rates than the non-LUT schemes, and in many cases even lower than the basic DFT-s-OFDM.* Moreover, the transition storing shows clearly lower computational complexity than the extrapolation, making the effect of using long filter impulse response negligible in terms of real additions compared with the short filter impulse response.

Regarding the computational complexity of conventional DFT-s-OFDM with WOLA, both multiplication and addition rates are only marginally higher than those of basic CP-OFDM. WOLA-based LUT schemes have somewhat lower addition rates than the corresponding short filter based schemes. The differences are negligible with transition storing and otherwise small, except for the single-tone case with group size of one and three-tone case with group size of three.

C. LUT wordlength requirements

The LUT-OFDM schemes are implemented in fixed-point finite-wordlength arithmetic considering worst-case scaling. In other words, the signal is scaled in such way that overflows do not occur. We focus here on the NB-IoT case, for which the requirements for in-band and out-of-band (OOB) emissions and EVM are specified by 3GPP [10]. The baseband model is

³The benefits of the decomposed scheme (DFT-s-OFDM-NB-D-FC) are marginal in the considered scenario, but they are expected to be more significant in allocations specific filtering of single- or three-tone signals.

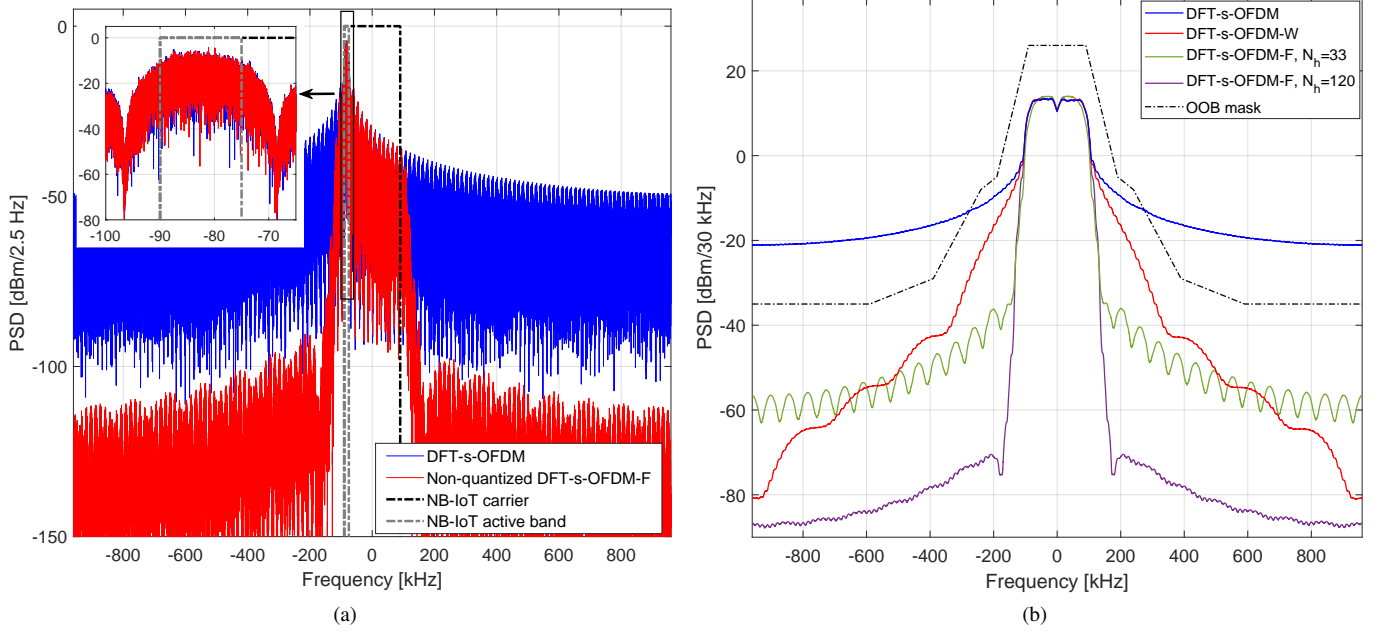


Fig. 10. (a) The PSDs of the transmitted non-quantized DFT-s-OFDM-F signal and the reference DFT-s-OFDM signal, showing also the positions of the NB-IoT carrier and the active tone. The shown PSD is an example of single-tone transmission with $\pi/2$ -BPSK and filter length $N_h = 120$. (b) PSDs of non-quantized twelve-tone cases of DFT-s-OFDM, DFT-s-OFDM-W, and DFT-s-OFDM-F with filter lengths $N_h = \{33, 120\}$.

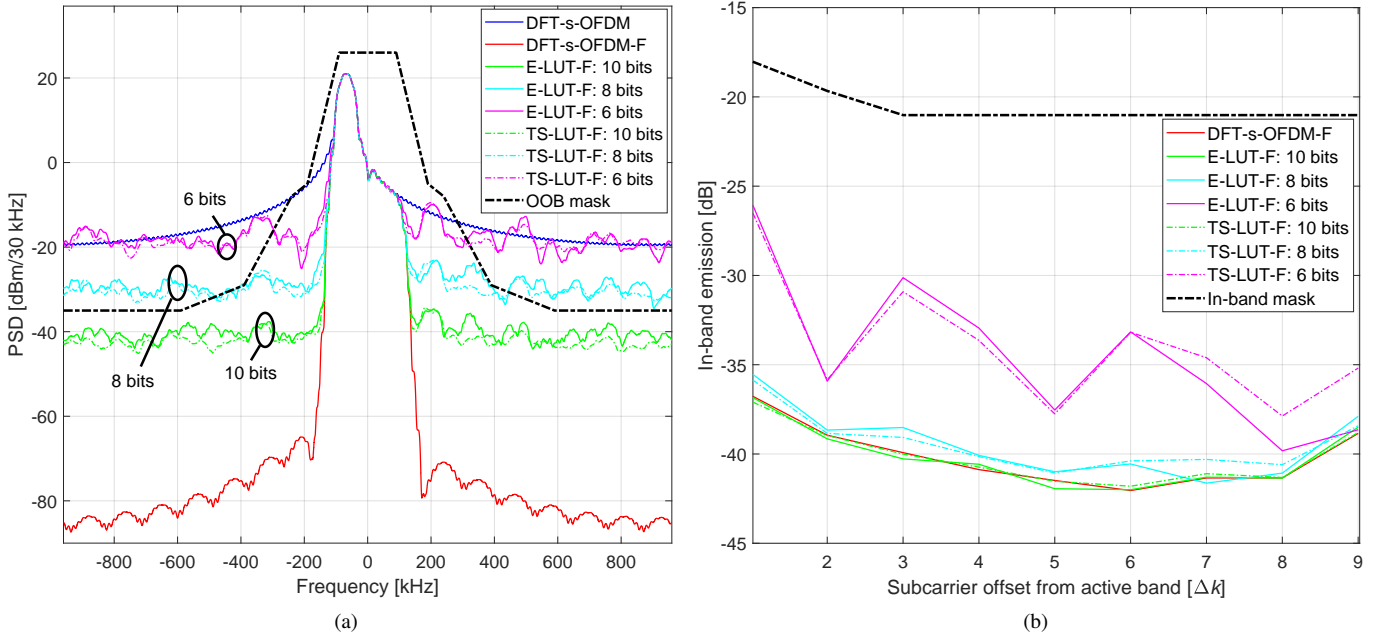


Fig. 11. (a) OOB and (b) in-band emissions for the three-tone case with group size of one with 6, 8, and 10 bit LUT wordlengths, QPSK modulation, filter length $N_h = 120$, and 22.5 dBm transmission power assuming linear PA. DFT-s-OFDM-F and DFT-s-OFDM are shown without quantization as references, along with the OOB and in-band emission masks of 3GPP specification [10].

used in the simulations and the active subcarriers are allocated at the edge of the NB-IoT channel of 12 subcarriers, in which case the OOB emission requirements are the most challenging. The maximum power of class-C NB-IoT devices is 23 dBm, while the maximum power reduction (MPR) of 0.5 dB, 1 dB, and 2 dB are allowed for three-tone, six-tone, twelve-tone cases, respectively, assuming that with less than 12 tones the allocation is at the edge of the channel [10].

Consequently, the following results are scaled to ensure the maximum power of 23 dBm, 22.5 dBm, 22 dBm, and 21 dBm, for single-tone, three-tone, six-tone, and twelve-tone cases, respectively. The spectral simulations have been carried out using the signal length of 50 subframes. Besides, for filtering based LUT-OFDM and DFT-s-OFDM-F, a root raised-cosine (RRC) filter with impulse response of length $N_h = 120$, 180 kHz wide passband, and 30 kHz transition bands are

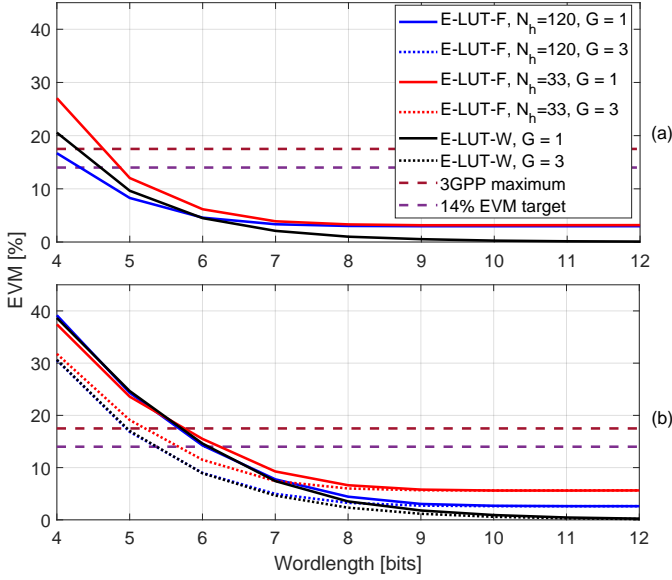


Fig. 12. EVM vs. wordlength in bits for different LUT implementations using WOLA-processing or filters of length $N_h = 120$ or $N_h = 33$ (a) for single-tone case with $\pi/2$ -BPSK modulation and (b) twelve-tone case with QPSK modulation.

used. Fig. 10(a) shows the PSD of single-tone DFT-s-OFDM-F and DFT-s-OFDM, indicating also the NB-IoT carrier and active subcarrier positions. Fig. 10(b) shows the PSDs of the considered DFT-s-OFDM variants for the twelve-tone case in the absence of quantization effects or power amplifier nonlinearities. In the following, the spectral characteristics are shown with different LUT wordlengths for QPSK modulation; with BPSK, the results are quite similar.

Fig. 11 shows the OOB and in-band emissions for basic and filtering based DFT-s-OFDM in the three-subcarrier case with group size of 1, filter length $N_h = 120$, and assuming linear power amplifier. The OOB emission results show leakage power outside the NB-IoT channel. The in-band emissions are measured from the unused subcarriers of the NB-IoT PRB, relative to the active subcarrier power, using an ideal DFT-s-OFDM-F receiver in noise-free case. The basic DFT-s-OFDM does not produce in-band interference in the considered idealized scenario and is not included in the figure. Generally, the OOB emissions of the basic DFT-s-OFDM based NB-IoT are always higher than the OOB mask at 23 dBm transmission power. Therefore, some additional signal processing is always required to satisfy the OOB emission requirements. On the other hand, the non-quantized F-OFDM and 10 bits LUT-OFDM satisfy the OOB and in-band emission masks. The minimum wordlength requirements for the OOB and in-band emissions are shown in Table IV. It was verified that the effects of CP extrapolation and transition storing are quite insignificant in all tested configurations. Generally, the required wordlength increases with increasing number of active subcarriers, while grouping relaxes the wordlengths requirements somewhat.

Figs. 12 shows the resulting EVM as a function of wordlength for single-tone cases with $\pi/2$ -BPSK and twelve-tone cases with QPSK. Following the 3GPP specifications,

TABLE IV
THE MINIMUM WORDLENGTHS REQUIRED TO REACH THE OOB AND IN-BAND EMISSIONS MASKS AND AT MOST 14 % EVM FOR DIFFERENT CP EXTRAPOLATION BASED LUT CONFIGURATIONS. THE UPPER NUMBERS REPRESENT WOLA-BASED LUT AND THE MIDDLE AND LOWER NUMBERS REPRESENT FILTER LENGTHS OF $N_h = \{33, 120\}$, RESPECTIVELY. SINGLE ENTRY INDICATES COMMON VALUE FOR ALL CASES.

Subband size	Group size	Wordlength limiting metric		
		OOB	In-band	EVM
1	1	10		
		10	4	5
		9		
3	1		5	
		10	6	6
			5	
	3	9	4	5
6	1		7	
		10	7	6
			6	
	3			5
		9	5	6
				5
12	1	10	–	7
		10	–	
		9	–	6
	3			
		10	–	

the received symbols are equalized to reduce the interferences that are caused by the filtering, especially due to non-ideal passband response. In any case, filtering harms the orthogonality of subcarriers, which is seen as non-zero EVM even without quantization in the filtering cases, in contrast to non-quantized WOLA. Additionally, a major cause of in-band interference is the finite-wordlength implementation of the transmitter processing, as seen after infinite-precision receiver processing. 3GPP specifications allow 17.5 % (15.2 dB) EVM with BPSK and QPSK modulations. In order to leave room for other transmitter non-idealities, we target at 14 % (20 dB) maximum EVM due to quantization and filtering effects. Generally, the longer filter and WOLA processing provide somewhat better EVM performance than the short filter. Also, input symbol grouping helps to reduce the LUT quantization effects on EVM. The resulting minimum wordlengths for different LUT configurations are shown in Table IV, indicating that wordlengths of 5 to 7 bits are sufficient to achieve the target EVM value. The results shown in Table IV indicate that the OOB emission mask is the most critical part of the specifications regarding the required LUT wordlength. The grouping of three input symbols reduces the minimum requirements by 1 bit in single-tone, three-tone, and six-tone cases. The resulting minimum wordlength defined by the OOB emission requirements is 9 or 10 bits.

D. Nonlinear power amplifier effects

Finally, a practical nonlinear power amplifier (PA) model is applied on LUT variants. The PA model is a memoryless AM-AM and AM-PM conversion model based on measurements of a commercial CMOS power amplifier for mMTC devices.

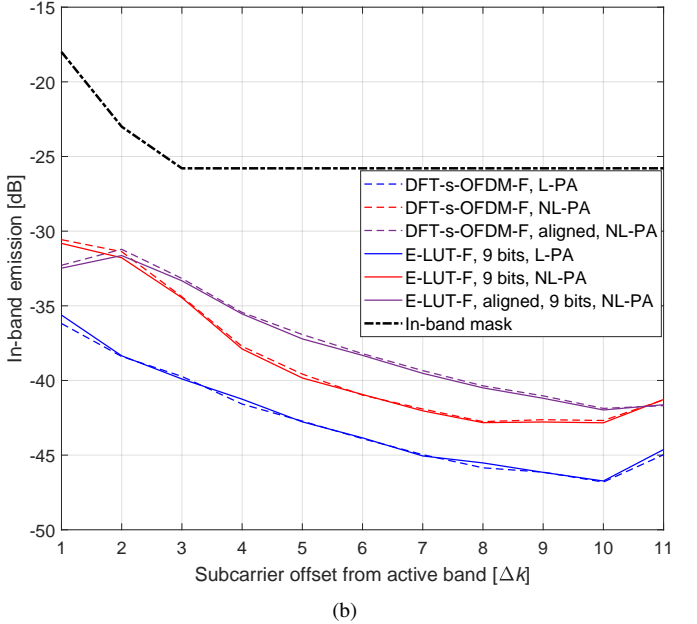
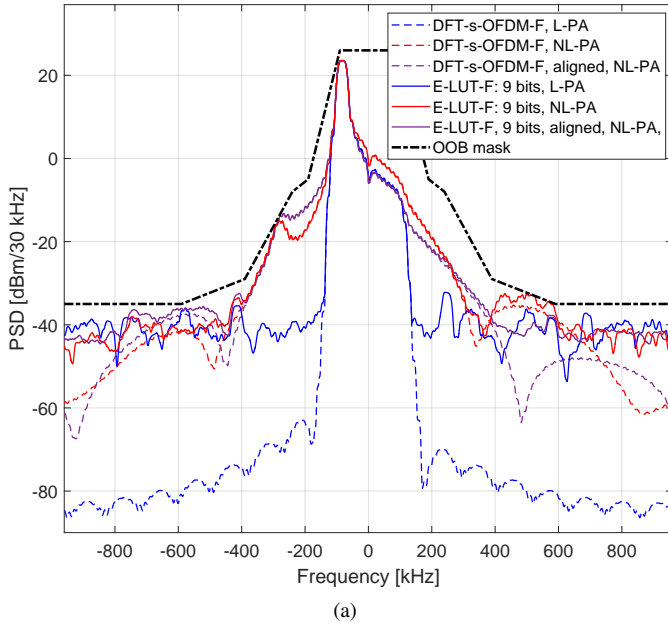


Fig. 13. The (a) OOB and (b) in-band emissions for the single-tone case with $\pi/2$ -BPSK modulation, filter length $N_h = 120$, 9 bit LUT wordlength, with and without phase alignment, and 23 dBm transmission power with linear (L-PA) and nonlinear PA (NL-PA) models. DFT-s-OFDM-F cases without quantization are shown for reference, along with the 3GPP emission masks [10].

Here, we check the PA nonlinearity effects with respect to the OOB and in-band emission masks. Fig. 13 shows the OOB and in-band emissions of filtering based LUT-OFDM for the single-tone case using the PA model, with infinite-precision DFT-s-OFDM as reference. Furthermore, Fig. 13 shows results for the single-tone case both with and without phase alignment. The results show that the quantized LUT-OFDM signal fulfills the OOB and in-band emission masks also with practical NB-IoT PA model. The effect of the PA nonlinearity can be observed clearly in the OOB results as an increase in the near OOB spectrum level. However, the effects of the PA nonlinearity further away from the active band are negligible when compared with the quantization error effects. Furthermore, the impact of phase alignment in the single-tone case is negligible compared with the non-aligned single-tone case for both infinite precision and 9 bits cases. With this particular single-tone allocation, the margin to the OOB emission mask is actually slightly reduced in the phase aligned case. When checking other possible single-tone allocations, we could not find clear systematic behavior in the OOB emission characteristics due to phase alignment. Accordingly, in future single-tone DFT-s-OFDM system developments, the potential benefits of phase alignment should be carefully evaluated, considering the greatly increased memory requirements in LUT-based implementations. The simulations show that, with the nonlinear PA model, the minimum wordlength requirement to satisfy the in-band emission mask increases to 7 bits and 8 bits for the three-tone and six-tone cases, both with group size of one. Nevertheless, the results shown in Table IV hold also with a practical PA model for the rest of the tone configurations. Especially, the most critical wordlength limitations due to OOB emissions are not affected by the used PA model.

Fig. 14 compares OOB emission of different LUT implementations considering also the short filter ($N_h = 33$) and WOLA-based LUT schemes. The results include the non-quantized LUTs with ideal PA as reference cases. Basically, LUT-based WOLA does not satisfy the OOB emission mask with nonlinear PA in the single-tone case. However, in multi-tone cases WOLA has sufficient margin to satisfy the emission mask with nonlinear PA. Generally, increasing filter length provides higher margin to the OOB emission mask and also the short filter case has significantly higher margin than WOLA at short distances from the active band. This indicates that with the used highly nonlinear PA model, an optimized filter based LUT design could allow larger transmit power than WOLA based LUT. The design and optimization of filters for LUT-OFDM is an interesting topic for future research.

VI. CONCLUSION

In this paper, efficient look-up-table (LUT) based schemes were developed for the digital baseband transmitter processing of narrowband IoT or mMTC devices. The proposed scheme allows ultra-low complexity on-line operation, after the complex evaluations of filtering and FFT/IFFT processes have been computed off-line and stored to the LUT. Based on matrix formalism for the filtered DFT-s-OFDM waveform, analytical expressions for the LUT computation were provided, along with expressions for the memory requirements and addition rates for different schemes. Multiplications can be completely avoided in these schemes and addition rates are clearly reduced compared to the time-domain filtering and fast-convolution based schemes. By constructing the LUT for groups of input symbols, the addition rate can be further reduced, with the cost of larger memory requirement. A simple cyclic prefix (CP) extrapolation scheme was applied for reducing the memory

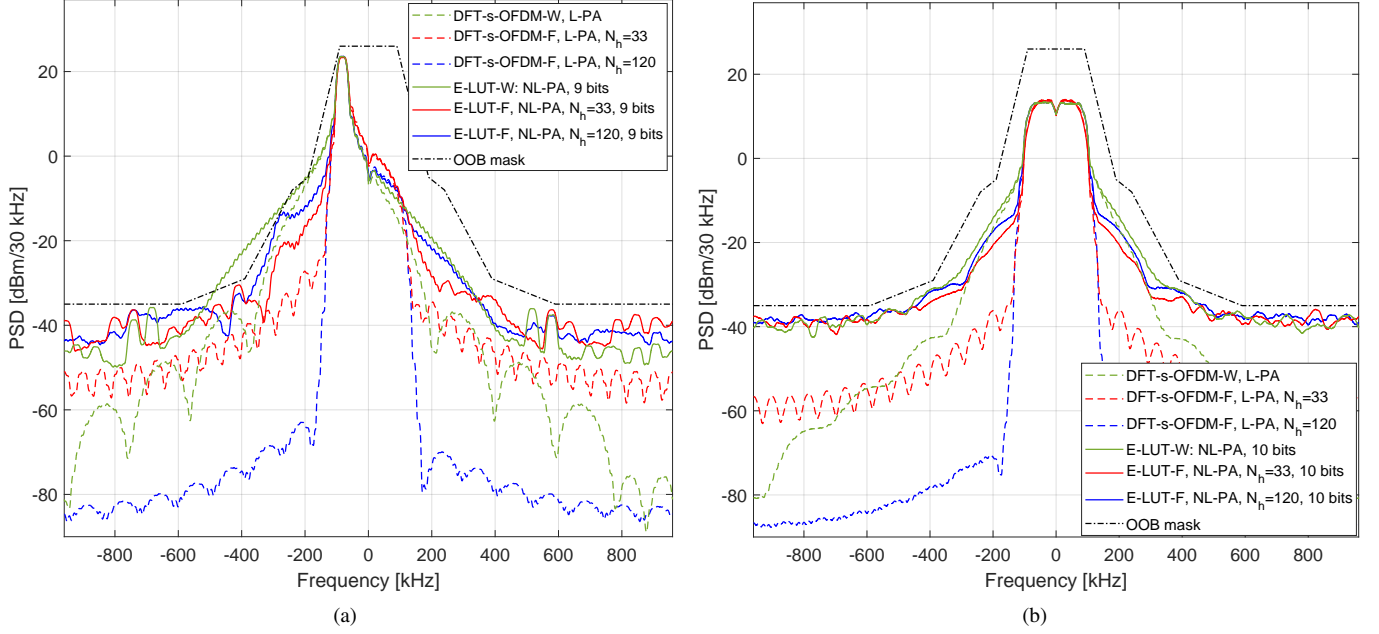


Fig. 14. OOB emissions with nonlinear PA (NL-PA) for WOLA and filtering based LUT implementations of DFT-s-OFDM. (a) Aligned single-tone case with $\pi/2$ -BPSK modulation and 9 bit LUT wordlength. (b) twelve-tone case with QPSK modulation and 10 bits LUT wordlength. The transmission powers are 23 dBm and 21 dBm for single-tone and twelve-tone cases respectively. Non-quantized cases with linear PA (L-PA) are shown for reference, along with the 3GPP emission mask [10].

requirements in cases where the CP lengths are variable within the transmission frame. Numerical comparisons were presented for different modulation orders, bandwidths, and group sizes, to identify configurations with reasonable memory requirements and low addition rates.

While this work concentrated on NB-IoT framework, the proposed LUT-based schemes are applicable to any low-rate mMTC physical layer processing where additional filtering is required to improve the spectral containment of the transmitted signal. The proposed LUT-based scheme was applied also for multiplication-free WOLA, indicating somewhat reduced LUT sizes and addition rates. However, even rather short filter lengths give clearly lower OOB emissions than WOLA at frequencies close to the active band, leading to reduced sensitivity to nonlinear power amplifier effects with minor increase in complexity.

The provided results also include performance comparisons with practical, highly nonlinear power amplifier model. This had minor effect on the wordlength requirements of the LUT-OFDM. Generally, when considering other potential narrow-band applications of the proposed scheme, LUT-OFDM has the capability to produce very clean spectrum with slightly higher LUT wordlengths (say 12 to 14 bits). In this case, the transmitted signal quality depends primarily on the the power amplifier linearity.

In this work, the minimum wordlengths were found by rounding the infinite-precision values. In future work, we consider optimizing the filter length and impulse response, along with the quantization wordlength with respect to the OOB requirements, expecting significant reduction in the minimum wordlength and LUT size.

APPENDIX A COMPUTATIONAL COMPLEXITY AND MEMORY REQUIREMENTS

Different LUT-OFDM variants have quite different memory requirements and real addition rates. The real addition rate can be divided into two parts, namely, the real additions for combining the sample vectors from multiple LUTs for each symbol of a subframe (α_s) and real additions for combining the overlapping parts of the symbol (α_f). Accordingly, the generic formula for the normalized real additions per processed BPSK/QPSK symbol is expressed as follows:

$$\alpha = \frac{1}{N_f B} (\alpha_f + \alpha_s). \quad (27)$$

Considering the basic LUT-OFDM, the required number of real additions per subframe is expressed as follows:

$$\alpha_s^{(1)} = 2(B-1)(N_t + (N_f - 1)N_h - N_f + 1) \quad (28a)$$

$$\alpha_f^{(1)} = 2(N_f - 1)(N_h - 1). \quad (28b)$$

The required number of memory elements for basic LUT-OFDM is expressed as

$$\epsilon_n^{(1)} = 2^o B (\hat{N}_c + N_c) \quad (29a)$$

$$\epsilon_e^{(1)} = 2^o B N_c, \quad (29b)$$

for normal CP configuration and extended CP configuration, respectively. Here \hat{N}_c is for the first symbol in the slot, N_c is for the rest of the symbols in the slot, and $o = 2$ for single subcarrier $\pi/4$ -QPSK and $o = 1$ otherwise.

Input symbol grouping based LUT-OFDM reduces required real additions approximately by the factor of G . This can be noticed in the following formula:

$$\alpha_s^{(2)} = 2 \left(\frac{B}{G} - 1 \right) (N_t + (N_f - 1)N_h - N_f + 1) \quad (30a)$$

$$\alpha_f^{(2)} = 2(N_f - 1)(N_h - 1). \quad (30b)$$

On other hand, the grouping increases exponentially the memory requirement by the factor P/G . Then, the memory requirement is expressed as

$$\epsilon_n^{(2)} = 2 \frac{BP}{G} (\hat{N}_c + N_c) \quad (31a)$$

$$\epsilon_e^{(2)} = 2 \frac{BP}{G} N_c, \quad (31b)$$

for normal CP configuration and extended CP configuration, respectively.

The CP extrapolated LUT targets at reducing the memory requirement for normal CP configuration. The extrapolation of the CP reduces the memory requirement by $2\hat{N}_c BP/G$. This accompanied with a reduction in real additions as

$$\alpha_s^{(3)} = 2N_f N_c \left(\frac{B}{G} - 1 \right) \quad (32a)$$

$$\alpha_f^{(3)} = 2 \left((N_f - 1)(N_h - 1) - \left(\frac{N_f}{N_b} - 1 \right) N_\Delta \right), \quad (32b)$$

where N_b is the number of DFT-s-OFDM-F symbols per slot, and $N_\Delta = \hat{N}_{cp} - N_{cp}$. The reduced memory requirement is expressed as follows:

$$\epsilon_n^{(3)} = 2^o \left(\frac{BP}{G} \right) N_c. \quad (33)$$

Transition storing based LUT-OFDM reduces the required real additions with the expense of increase in the memory requirements. The number of real additions per subframe is expressed as follows:

$$\alpha_s^{(4)} = 2 \left(\frac{B}{G} - 1 \right) (N_t - N_\Delta). \quad (34)$$

Here, the filtering overlapping is already calculated and stored. Therefore, the additions of filter overlapping do not appear in the formula. Subsequently, the memory requirements are expressed as

$$\epsilon_n^{(4)} = \epsilon_n^{(3)} + 2^o \frac{BP'}{G} (2N_h - N_\Delta - 2) \quad (35a)$$

$$\epsilon_e^{(4)} = \epsilon_e^{(3)} + 2^o \frac{BP'}{G} (N_h - 1), \quad (35b)$$

for normal CP configuration and extended CP configuration, respectively.

REFERENCES

- [1] A. Loulou, J. Yli-Kaakinen, T. Levanen, V. Lehtinen, F. Schaich, T. Wild, M. Renfors, and M. Valkama, "Look-up table based implementation of ultra-low complexity narrowband OFDM transmitters," in *Proc. 2019 16th International Symposium on Wireless Communication Systems (ISWCS 2019)*, Oulu, Finland, Aug. 2019.
- [2] D. Soldani and A. Manzalini, "Horizon 2020 and beyond: On the 5G operating system for a true digital society," *IEEE Vehicular Technology Magazine*, vol. 10, no. 1, pp. 32–42, Mar. 2015.
- [3] J. Chen, K. Hu, Q. Wang, Y. Sun, Z. Shi, and S. He, "Narrowband internet of things: Implementations and applications," *IEEE Internet of Things Journal*, vol. 4, no. 6, pp. 2309–2314, Dec. 2017.
- [4] R. Ratasuk, N. Mangalvedhe, Y. Zhang, M. Robert, and J. P. Koskinen, "Overview of narrowband IoT in LTE Rel-13," in *Proc. 2016 IEEE Conference on Standards for Communications and Networking (CSCN)*, Oct. 2016, pp. 1–7.
- [5] Y. E. Wang, X. Lin, A. Adhikary, A. Grovlen, Y. Sui, Y. Blankenship, J. Bergman, and H. S. Razaghi, "A primer on 3GPP narrowband internet of things," *IEEE Communications Magazine*, vol. 55, no. 3, pp. 117–123, Mar. 2017.
- [6] J. Xu, J. Yao, L. Wang, Z. Ming, K. Wu, and L. Chen, "Narrowband internet of things: Evolutions, technologies, and open issues," *IEEE Internet of Things Journal*, vol. 5, no. 3, pp. 1449–1462, Jun. 2018.
- [7] Y. Miao, W. Li, D. Tian, M. S. Hossain, and M. F. Alhamid, "Narrowband internet of things: Simulation and modeling," *IEEE Internet of Things Journal*, vol. 5, no. 4, pp. 2304–2314, Aug. 2018.
- [8] S. Parkvall, E. Dahlman, A. Furuskar, and M. Frenne, "NR: The new 5G radio access technology," *IEEE Communications Standards Magazine*, vol. 1, no. 4, pp. 24–30, Dec. 2017.
- [9] T. Levanen, J. Pirskanen, K. Pajukoski, M. Renfors, and M. Valkama, "Transparent Tx and Rx waveform processing for 5G new radio mobile communications," *IEEE Wireless Communications*, vol. 26, no. 1, pp. 128–136, Feb. 2019.
- [10] *User Equipment (UE) radio transmission and reception (Release 15)*, 3GPP TS 36.101, Mar. 2018, v15.2.0.
- [11] R. Ratasuk, J. Tan, N. Mangalvedhe, M. H. Ng, and A. Ghosh, "Analysis of NB-IoT deployment in LTE guard-band," in *2017 IEEE 85th Vehicular Technology Conference (VTC Spring)*, Jun. 2017, pp. 1–5.
- [12] *Mobile IoT in the 5G future*, GSMA, Apr. 2018.
- [13] R. Zayani, Y. Medjahdi, H. Shaiek, and D. Roviras, "WOLA-OFDM: A potential candidate for asynchronous 5G," in *Proc. 2016 IEEE Globecom Workshops (GC Wkshps)*, Dec. 2016, pp. 1–5.
- [14] J. Abdoli, M. Jia, and J. Ma, "Filtered OFDM: A new waveform for future wireless systems," in *Proc. 2015 IEEE 16th International Workshop on Signal Processing Advances in Wireless Communications (SPAWC)*, Jun. 2015, pp. 66–70.
- [15] V. Vakilian, T. Wild, F. Schaich, S. ten Brink, and J. F. Frigon, "Universal-filtered multi-carrier technique for wireless systems beyond LTE," in *Proc. IEEE Globecom Workshops (GC Wkshps)*, Dec. 2013, pp. 223–228.
- [16] J. Li, E. Bala, and R. Yang, "Resource block filtered-OFDM for future spectrally agile and power efficient systems," *Physical Communication*, vol. 11, pp. 36 – 55, 2014.
- [17] L. Zhang, A. Ijaz, P. Xiao, M. M. Molu, and R. Tafazolli, "Filtered OFDM systems, algorithms, and performance analysis for 5G and beyond," *IEEE Transactions on Communications*, vol. 66, no. 3, pp. 1205–1218, Mar. 2018.
- [18] J. Yli-Kaakinen, T. Levanen, S. Valkonen, K. Pajukoski, J. Pirskanen, M. Renfors, and M. Valkama, "Efficient fast-convolution-based waveform processing for 5G physical layer," *IEEE Journal on Selected Areas in Communications*, vol. 35, no. 6, pp. 1309–1326, Jun. 2017.
- [19] A. Loulou, J. Yli-Kaakinen, and M. Renfors, "Efficient fast-convolution based implementation of 5G waveform processing using circular convolution decomposition," in *Proc. 2017 IEEE International Conference on Communications (ICC)*, May 2017, pp. 1–7.
- [20] T. Okano, M. Umehira, X. Wang, and S. Takeda, "Overlap-windowed-DFTs-OFDM with overlap FFT filter-bank for flexible uplink access in 5G and beyond," in *2018 IEEE 88th Vehicular Technology Conference (VTC-Fall)*, Aug. 2018, pp. 1–6.
- [21] F. Schaich, T. Wild, R. Ahmed *et al.*, "Deliverable D3.1: Preliminary results for multi-service support in link solution adaptation," Project: Flexible Air iNTerfAce for Scalable service delivery wiThIn wireless Communication networks of the 5th Generation (FANTASTIC-5G), Tech. Rep., May 2016.
- [22] F. Schaich and T. Wild, "Method of and apparatus for providing a sample vector representing at least a portion of a multi-carrier modulated signal," Patent application EP3 136 200A1, 2017.
- [23] E. Dahlman, S. Parkvall, and J. Sköld, *4G: LTE/LTE-Advanced for Mobile Broadband (Second Edition)*. Oxford: Academic Press, 2014.
- [24] *Technical Specification Group Radio Access Network (Release 15)*, 3GPP TS 36.211, Jun. 2018, v15.2.0.
- [25] *Definition of phase alignment for NB-IoT single tone UL modulation*, 3GPP TSG RAN1 NB-IoT Ad-Hoc meeting, Mar. 2016, r1-161857.